Collisionless Electron Dynamics in the Magnetosheath of Mars

S. J. Schwartz, L. Andersson, S. Xu, D. L. Mitchell, H. Akbari, R. E. Ergun, C. Mazelle, S. A. Thaller, A. R. N. Sales, K. Horaites, et al.

AGU100 ADVANCING EARTH AND SPACE SCIENCE

Geophysical Research Letters

RESEARCH LETTER
10.1029/2019GL085037

Key Points:
- This study develops an idealized collisionless model for electrons in Mars's magnetosheath
- The model reproduces the erosion of higher energy electron phase space within the magnetosheath

Supporting Information:
- Supporting Information S1

Correspondence to:
S. J. Schwartz,
steven.schwartz@lasp.colorado.edu

Citation:
Schwartz, S. J., Andersson, L., Xu, S., Mitchell, D. L., Akbari, H., Ergun, R. E., et al. (2019). Collisionless electron dynamics in the magnetosheath of Mars. *Geophysical Research Letters*, *46*, 11,679–11,688. https://doi.org/10.1029/2019GL085037

Received 16 AUG 2019
Accepted 21 SEP 2019
Accepted article online 29 OCT 2019
Published online 7 NOV 2019

Collisionless Electron Dynamics in the Magnetosheath of Mars

S. J. Schwartz[1,2], L. Andersson[1], S. Xu[3], D. L. Mitchell[3], H. Akbari[1], R. E. Ergun[1], C. Mazelle[4], S. A. Thaller[1], A. R. N. Sales[1], K. Horaites[1], G. A. DiBraccio[5], and K. Meziane[4,6]

[1]Laboratory for Atmospheric and Space Physics, University of Colorado Boulder, Boulder, CO, USA, [2]Also Emeritus at Blackett Laboratory, Imperial College London, London, UK, [3]Space Science Laboratory, University of California Berkeley, Berkeley, CA, USA, [4]IRAP CNRS-University of Toulouse-UPS-CNES, Toulouse, France, [5]NASA Goddard Space Flight Center, Greenbelt, MD, USA, [6]Physics Department, University of New Brunswick, Fredericton, New Brunswick, Canada

Abstract Electron velocity distributions in Mars's magnetosheath show a systematic erosion of the energy spectrum with distance downstream from the bow shock. Previous attempts to model this erosion invoked assumptions to promote electron ionization impact collisions with Mars's neutral hydrogen exosphere. We show that the near collision-free magnetosheath requires a kinetic description; the population of electrons at any location is a convolution of electrons arriving from more distant regions that ultimately map directly to the solar wind. We construct a simple model that captures all the essential physics. The model demonstrates how the erosion of the electron distributions is the result of the trapping, escape, and replacement of electrons that traverse the global bow shock; some are temporarily confined to the expanding cavity formed by the cross-shock electrostatic potential. The model also has implications for the ability of solar wind electrons to reach altitudes below the pileup boundary.

Plain Language Summary All the planets are embedded in a supersonic flow of ionized gas originating from the Sun's hot atmosphere. Thus, upstream of a planet we see shock waves that slow, heat, and divert the flow around the planet. At planets such as Mars, which lack an internal magnetic field, that shock and the sheath of diverted flow are quite close to the top of the atmosphere. Thus, it has been tempting to attribute the evolution of the gas within the sheath by invoking collisions between, for example, the shocked solar wind electrons and neutral constituents from the planet. However, such collisions are actually quite infrequent. We have developed a simple collision-free model that shows how the apparent reduction in energy of the shocked solar wind electrons is the result of electron escape back into the exterior flow and their effective replacement by less energized electrons. This approach also highlights the ability of exterior electrons to penetrate more deeply into the atmosphere.

1. Introduction

Supersonic flows are common in astrophysical environments. Their interaction with slow flows or other obstacles results in the formation of a shock wave. In the predominantly collision-free cosmos, such shocks are believed to be responsible for important nonthermal processes, including the acceleration of particles to high energies. Within the solar system, shocks are directly accessible for measurements by in situ instrumentation on spacecraft. Results from the terrestrial bow shock, and that from other planets and traveling interplanetary shocks, have elucidated many of the key physical processes and provided inspiration and ground truth for a range of numerical simulational models (see for a review Burgess & Scholer, 2015).

Not all bow shocks are the same. At planets with a significant intrinsic dipole field, such as Earth, Jupiter, and Saturn, it is the magnetic pressure that ensures the bow shock stands off 10 or more planetary radii from the surface. The gross behavior in these systems resembles fluid-like models of supersonic flow around an obstacle, albeit with attendant particle acceleration and turbulence not captured by a fluid treatment.

At smaller, unmagnetized bodies such as comets, the interaction is dominated by kinetic effects and polluted by copious numbers of newly ionized particles that originate in the body's neutral atmosphere and get picked up by the solar wind flow. The extended interaction resembles its larger planetary cousins but is much

richer in plasma kinetic processes and more complex than the textbook shock wave propagating through a homogeneous medium (Glassmeier, 2017).

Mars is a more substantial obstacle, in which pick up of newly ionized particles also has an impact on the interaction of the solar wind. The lack of a global intrinsic field shrinks the shock stand-off distance to less than a Martian radius above the planetary surface (Trotignon et al., 2006; Vignes et al., 2000). The pressure is supplied by the combination of the Martian ionosphere and crustal magnetic fields, with the interplanetary field forming a "magnetic pileup boundary" (MPB) that roughly plays the role of the magnetopause at magnetized planets. Studies of this system have been reinvigorated (Gruesbeck et al., 2018; Hall et al., 2019; Mazelle et al., 2018; Meziane et al., 2017, 2019) by the detailed data being returned by the MAVEN mission, including high-quality in situ particle and field measurements, for example (Dubinin et al., 2018; Elliott et al., 2013).

Although shock waves in interplanetary space have underpinned our understanding of collisionless shocks, the parameter regimes found there are somewhat limited, with some important exceptions at Saturn (Masters et al., 2011, 2013). Ghavamian et al. (2013) made direct comparisons between the properties at interplanetary shocks and supernova remnants. An often overlooked aspect is that the solar wind flow, while being much faster than typical magnetosonic wave speeds and the ion thermal speeds, is almost always much less than the electron thermal speed. We discuss below how the sea of highly mobile, nearly collision-free electrons has global consequences for our understanding of the Martian bow shock.

Electron spectra in the Martian magnetosheath region between the bow shock and MPB were studied by Crider et al. (2000). They found that the inflated electron velocity space distributions found behind the bow shock were eroded in energy, most noticeably in a systematic fashion at and through the MPB. They postulated that this erosion was the result of cascading energy loss through electron impact ionization of Mars's extended neutral hydrogen exosphere. Acknowledging that the electron speed is much faster than the flow speed, they constructed a model for the slowdown of the field lines to ~5 km/s so that, at lowest altitude, electrons might spend 425 s interacting with a 10^6/cc neutral hydrogen population. For reference, a 60-eV electron has a mean free path ~60 R_{mars} in such an environment. Implicit in the Crider et al. (2000) model is some confinement along the field lines in a fluid element-like fashion, since otherwise electrons might be expected to leave the MPB environment before suffering the necessary ~10 collisions with neutral hydrogen. This provides us the motivation to consider the collisionless kinematics of electrons in the global Martian magnetosheath.

The access to the Martian atmosphere of solar wind plasma has important consequences for the energy deposition at high altitudes (Sakai et al., 2016) where atmospheric loss of selected species is more efficient than from lower, collision-dominated regions where any deposited energy would be shared and thermalized (Ergun et al., 2016). Matsunaga et al. (2015) studied episodes of penetration to altitudes <400 km of shocked magnetosheath plasma. They attributed these phenomena to plasma transport/exchange by Kelvin-Helmholtz instabilities under specific interplanetary conditions.

In this paper, we explore the limiting case of totally collision-free magnetosheath electron behavior. The foundations for our approach were laid out by Feldman et al. (1983), who examined the pitch angle distributions of electrons at various locations around the Earth's bow shock and within the sheath. They noted that to preserve neutrality, lower-energy sheath electrons must be retained by an electrostatic well established at the global bow shock. Higher-energy sheath electrons traveling along the field overcome the shock potential and escape across the bow shock as the field lines to which they are tied are advected further downstream. This loss continues as the shock strength, and potential, weakens with distance from the subsolar regions. They also documented systematic variations of anisotropies and asymmetries along with other features of electron beams seen within the shock transition and flat-topped distributions further downstream.

In a series of papers, Mitchell et al. (2012) and Mitchell and Schwartz (2013, 2014; hereafter MS) showed that characteristic features of the electron velocity spectra are common across large distances in the terrestrial magnetosheath (Mitchell et al., 2012), implying little ongoing spectral modification despite the presence of, for eample, large-amplitude whistler turbulence. They then constructed (Mitchell & Schwartz, 2013) and tested (Mitchell & Schwartz, 2014) a detailed self-consistent global model for the bow shock and sheath flow together with the electron kinetics, showing that the electron distribution at any location (except the point where the interplanetary magnetic field is tangent to the shock) is the convolution of electrons arriving from

the solar wind via a large swath of locations around the curved shock surface. This process supplies accelerated solar wind electrons, traps them, lets them escape and resupplies electrons as a given field line advects antisunward. Their conclusion that the resulting electron "heating" is an intrinsically nonlocal process is a consequence of both the collisionless nature of the plasma and the highly mobile sea of interplanetary electrons described above. Although MS focused on the electron distributions at the shock surface itself, the concepts developed there reveal that the distributions measured at any point within the magnetosheath will be a convolution of electrons arriving from a vast range of locations around the shock.

In the present paper, we construct a very simplified kinematic model of electrons within the Martian magnetosheath that captures all the essential physics from MS, although it taps the result for the variation of the shock potential rather than deduce it self-consistently. In essence, the shock potential is large at the subsolar shock and efficiently confines most of the electron population. Those confined electrons lose energy at every encounter with the bow shock, a result of the lengthening of the field line on which they reside. As the field lines convect toward the MPB, however, the field lines connect to the shock further along its flanks where the potential is weaker. More energetic magnetosheath electrons are able to escape there and are replaced by incoming ambient solar wind electrons that experience less acceleration by the weaker potential.

The next section presents some MAVEN electron distributions to illustrate the erosion reported by Crider et al. (2000). Subsequent sections outline the model for the fields, flow, and electron kinetics. Mathematical details of the model can be found in the supporting information (SI). We then show some model results and draw conclusions.

2. Data and Observations

We draw on electron data from the Solar Wind Electron Analyzer (SWEA) instrument aboard MAVEN (Mitchell et al., 2016). SWEA is a hemispherical electrostatic analyzer with deflectors that measures the energy-angle distribution of electrons from 3 eV to 4.6 keV with an energy resolution (dE/E) of 17% and an angular resolution of ~20°. The field of view, spanning 80% of the sky, is mapped into pitch angles onboard to produce energy-pitch angle distributions as rapidly as every 2 s. We show for context a spectrogram from the Solar Wind Ion Analyzer (SWIA; Halekas et al., 2015) that combines data from its onboard survey spectra and a 3-D coarse spectrum averaged over angles. We also show magnetometer data (Connerney et al., 2015) reduced from 32 vectors/s to 8-s resolution.

Figure 1 shows a 30-min traversal of the Martian bow shock and magnetosheath near noon local time under steady interplanetary conditions dominated by B_y. Panel (c) shows the electron phase space density at four energies (each averaged over several energy channels). These show a clear drop off in phase space density that commences in the middle of the magnetosheath for 250 eV electrons, with the drop off occurring progressively closer to the MPB at lower energies. The sequences of cuts in (e)–(g) show 1-D cuts of the electron distribution function $f(E)$, approximately corrected for spacecraft potential, along, antiparallel and perpendicular to the magnetic field averaged over the time intervals shown in the top panels. The dark red trace, at lower-energy resolution, was taken 3 min earlier when the solar wind was less contaminated by the influence of the bow shock and pick up ions. Energies below ~20 eV in the magnetosheath are contaminated by secondary electrons internal to the instrument. The apparent upturn near the 60-eV edge of $f(E)$ could be an artifact caused by overcorrecting the largest count rates for dead time.

The cuts at the bottom of Figure 1 show the inflation of the distribution to a flat-top-like shape at the bow shock and its steady degradation through the magnetosheath. Near the MPB at 13:47 it has returned to roughly the ambient solar wind levels. This pattern mimics that reported by Crider et al. (2000), although it emphasizes the systematic evolution through the entire magnetosheath, as discussed in relation to panel (c), rather than just that closer to the MPB.

3. Model: Fields and Flow

Figure 2 illustrates all the components of our simplified model. We assume the solar wind flow is incident along the X axis and that the interplanetary magnetic field is transverse to that direction. Other geometries would require more extensive modeling without changing the underlying qualitative behavior. For mathematical convenience we fit the Vignes et al. (2000) bow shock model with a parabola (both are shown in the

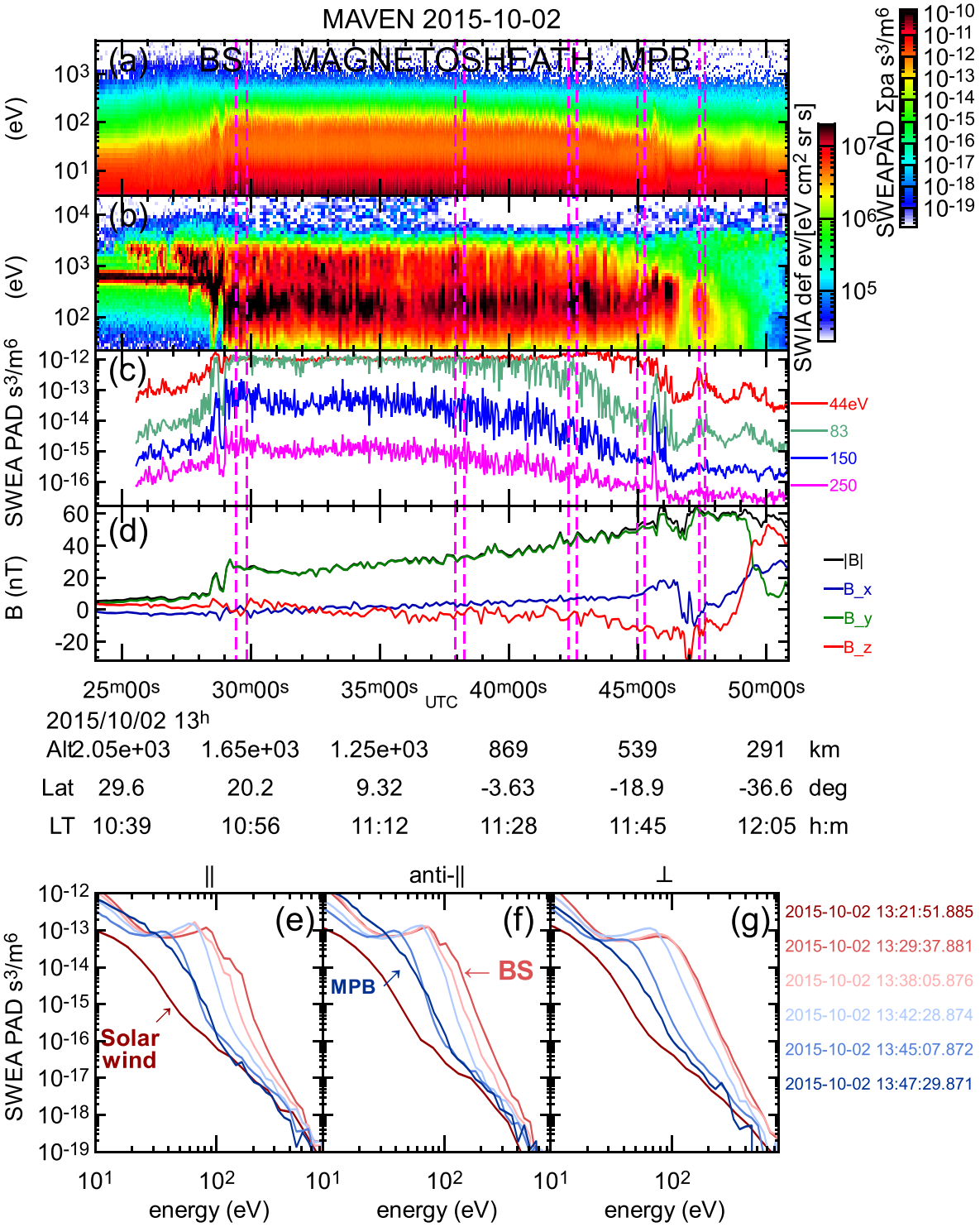

Figure 1. A traversal of the near-subsolar (Local Time near noon) Martian magnetosheath from the solar wind on the left through the bow shock at 13:29 to the magnetic pileup boundary near 13:46 on 2 October 2015. (top) Energy-time spectrograms of MAVEN high-resolution omnidirectional (a) electrons and (b) ions. Panel (c) shows line spectra of the electron omniirectional phase space density averaged over several channels around selected energies. The magnetic field in MSO coordinates is shown in (d). The field, mainly in the *Y* direction, appears to correspond to relatively steady interplanetary conditions. (bottom) 1-D cuts of the electron pitch angle distribution in directions (e) parallel, (f) antiparallel, and (g) perpendicular to the local field averaged over the different time intervals delineated by dashed lines in the top panels. The solar wind traces are cuts taken in lower resolution 3 min earlier when the spacecraft was further away from the contamination of the bow shock.

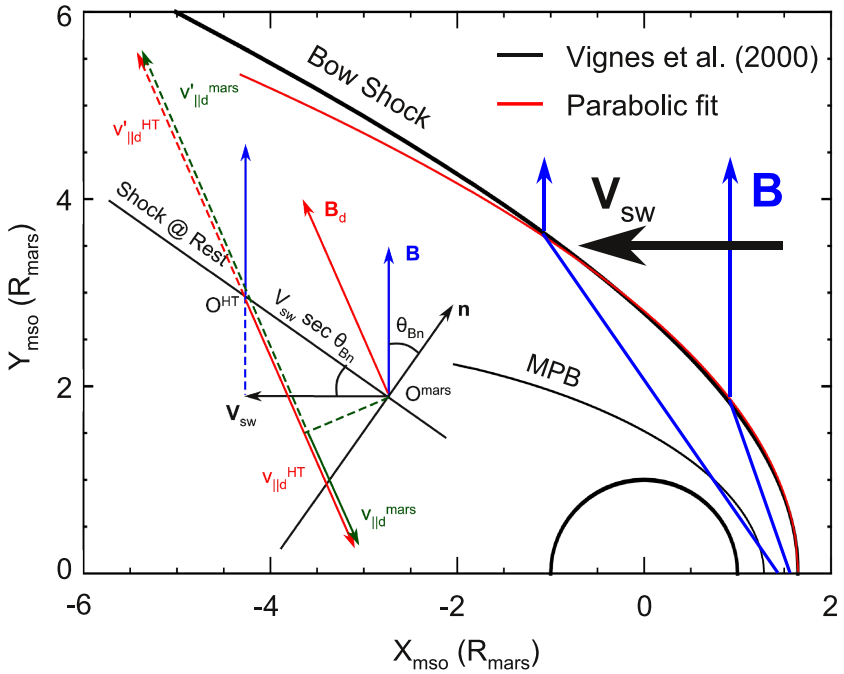

Figure 2. Illustration of the main elements of the model developed in this paper. The main figure shows the field and flow configuration, while the inset highlights the local velocity space transformation to the shock deHoffmann-Teller (dHT) frame (de Hoffmann & Teller, 1950) in which the shock is at rest and the bulk flow velocity is field aligned, so that the convective $-\mathbf{V}\times\mathbf{B}$ electric field is zero. In this frame, particle energy is conserved including the possible contributions of the ambipolar cross-shock potential ϕ^{HT} in the event that the particle traverses the shock.

figure). This configuration is symmetric about the X axis and we implicitly reflect particles and fields here as appropriate.

Along the X axis we impose a stagnation flow that decreases from its postshock value (assumed to be 0.3 times the solar wind speed $V_{\mathrm{SW}} = 450$ km/s) linearly to zero at the MPB (e.g., Spreiter et al., 1970). The thickness Δ of the sheath along this line is $0.37\,R_{\mathrm{mars}}$ from the MPB stand-off at $x = R_{\mathrm{MPB}} = 1.28R_{\mathrm{mars}}$ to the bow shock at $x = R_{\mathrm{BS}} = 1.65R_{\mathrm{mars}}$ (Vignes et al., 2000). A field line is tied to this stagnating flow at its intersection with the X axis.

The other end of the field line is frozen into the external solar wind flow and advects in the antisunward direction at the solar wind speed V_{SW}. We connect these two ends with a straight line. While the real fields are draped around the MPB by the full sheath flow pattern, we will focus on field-aligned electrons, which are tied to individual field lines because of their small gyroradii. The simple model here captures electron trajectories within the sheath to the extent that the lengthening straight field segments mimic semiquantitatively the lengthening curved field lines of the sheath. A parabolic draping shape would increase the length of the field line intersecting at $y = 5R_{\mathrm{mars}}$ by 35%; more sunward field lines less so.

With these assumptions, the locations of the ends of these field line segments can be solved analytically as functions either of time or of distance of the footpoint on the X axis. The electron behavior at the bow shock is performed in a local deHoffmann-Teller frame (dHT) (de Hoffmann & Teller, 1950). All our mathematics is given in SI, summarized below.

We also specify the ambipolar dHT electrostatic potential at the bow shock, ϕ^{HT}. The self-consistent model in MS found that this potential varied as $\sec\theta_{Bn}$ where θ_{Bn} is the local angle between the magnetic field and shock normal. In our model, this angle increases to 90° at the subsolar point. Empirically, ϕ^{HT} scales with the incident solar wind ram energy (Schwartz et al., 1988; Thomsen et al., 1987), that is, as $\cos^2$ of the angle between the flow velocity and shock normal. With our adopted geometry this dependency is $\propto \sin^2\theta_{Bn}$. Thus, the potential falls off with distance from the subsolar point. Accordingly, we specify

$$\phi^{\mathrm{HT}} = \phi_o \sin^2\theta_{Bn} \sec\theta_{Bn} \tag{1}$$

We take $e\phi_o = 0.1 m_p V_{SW}^2/2$ based on the same empirical results, although the potential at Mars may be weaker (Meziane et al., 2019). Changing this value has a quantitative impact on how close to the stagnation point an observer needs to be to be connected to the shock at a specific potential. This, and our other assumption of flow pattern and straight field lines, have no qualitative bearing on our results. The model breaks down in the immediate vicinity of the point of tangency (the subsolar point in our model) as noted by MS. In our treatment of the particle trajectories (next section) no observed particles can enter the magnetosheath there.

4. Model: Electron Kinetics

For illustrative purposes, in this letter we consider only particles with zero magnetic moment. This enables us to focus on electron entry, guiding center motion and energetics by looking only at the behavior of the parallel velocity $v_{||}$, which greatly simplifies the calculations.

Figure 2 also shows in an inset the local analysis at an intersection with the bow shock. This diagram is in velocity space. At the bow shock, the electron physics is greatly simplified by transforming to the dHT frame, where a magnetized electron preserves its magnetic moment and total energy, so that in our case a field-aligned electron remains so. Changes in its kinetic energy depend only on if, and in which direction, it traverses ϕ^{HT}. Within the sheath there is no change to a field-aligned electron's energy in a frame at rest with Mars (there are no perpendicular drifts parallel to the convective electric field which would exist there).

Consider the dashed green velocity vector $v'_{||d}{}^{mars}$ as seen in the Mars rest frame. In this frame there is also a perpendicular velocity component, but it does not enter into any of our calculations. Transforming to the dHT frame shifts the origin to O^{HT} in which the electron has a purely field-aligned velocity $v'_{||d}{}^{HT}$ shown by the dashed red trace. If the electron is unable to overcome the dHT potential, it will reflect in the dHT frame and return toward the X axis with a velocity $v_{||d}^{HT}$ shown as the solid red arrow. Shifting back to the Mars frame we see that the new electron velocity is $v_{||d}^{mars}$ (solid green arrow), which is shorter than its preencounter $v'_{||d}{}^{mars}$. The electron has lost energy due to the motion, or lengthening, of the field line as encapsulated in the dHT transformation.

On the other hand, if the electron arrives at the shock from the magnetosheath with sufficient energy in the dHT frame to overcome ϕ^{HT} it will traverse the shock, lose $e\phi^{HT}$ in energy, and become part of the solar wind electron population.

In practice, we follow electron trajectories backward in time, from a specified observer's location on the stagnation line for some arrival energy E_{obs}. Figure S1 in the SI displays a flow chart of our approach. At each encounter with the bow shock we ask whether that particle has more energy than $e\phi^{HT}$ in the dHT frame. If not, it must have been reflected so we reverse its motion back to the stagnation line, reflect it there, and continue.

If the electron at the bow shock does have more energy than $e\phi^{HT}$, it must have crossed the bow shock at that location from the solar wind. In this case we perform the dHT energetics to determine its energy E_{SW} in the solar wind. Liouville's Theorem applied to these 0° pitch angle electrons then implies that the phase space density of this energy in the solar wind must be the same as the phase space density at the observation point for the initial energy we considered there. That is,

$$f_{obs}(E_{obs}) = f^{SW}(E_{SW}) \tag{2}$$

Repeating this process for a full range of energies E_{obs} at the observer's location thus enables us to determine $f_{obs}(E)$. We use a Kappa velocity distribution for f^{SW}, with $\kappa = 3.5$ and $T = 10$ eV, as representative of typical solar wind electron distributions (Feldman et al., 1975; Pierrard & Lazar, 2010).

The mathematical details are given in the accompanying SI. We note here that the configuration and analysis provides analytical expressions for the field line endpoints and the time it takes for the electrons to traverse the individual segments, so that we do not need to do any detailed trajectory time-stepping calculations. The power of the Liouville mapping technique employed here is substantial.

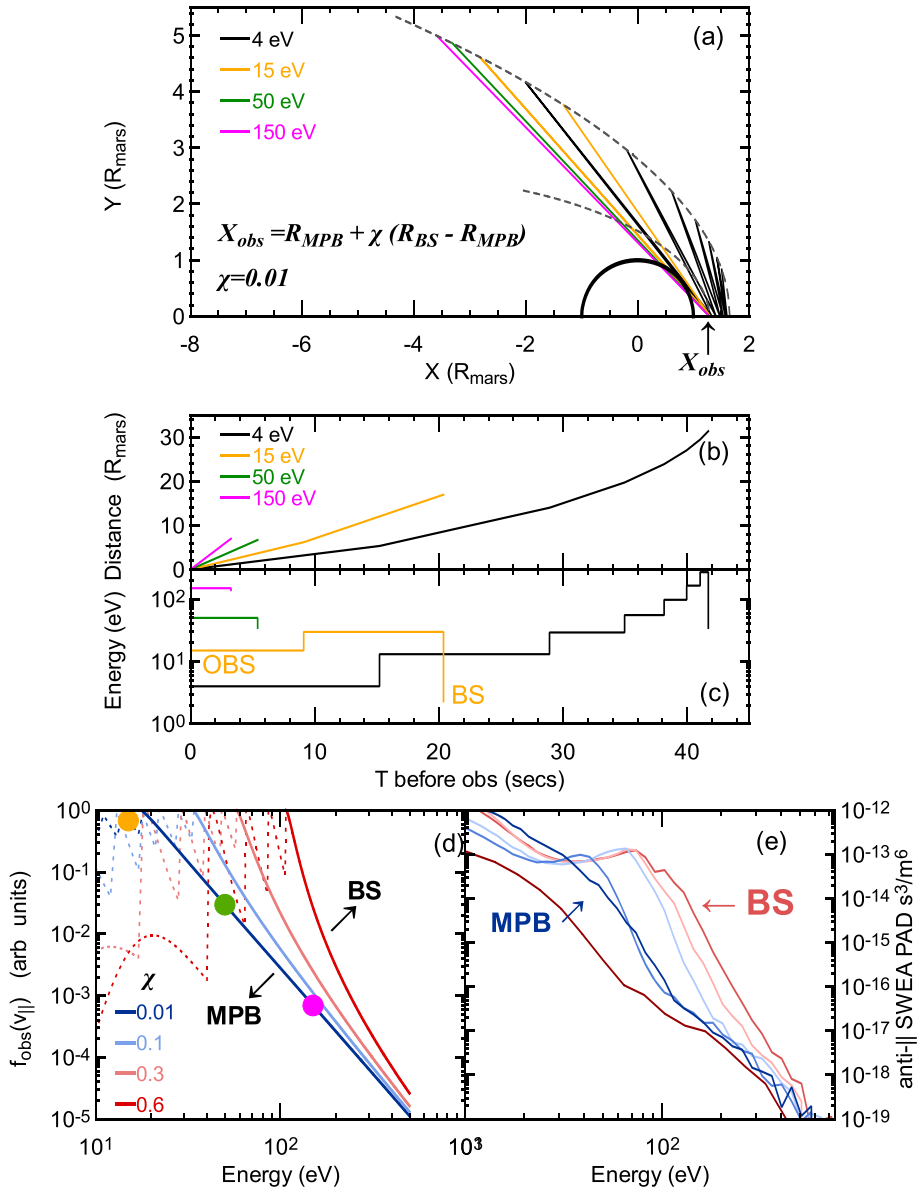

Figure 3. Model results. (a) Representative electron trajectories for electrons arriving at an observer's location 1% away from the stagnation point at the MPB, i.e., at $\chi = 0.01$. The actual trajectories would be curved due to field line advection in the sheath, but we have simplified this figure by straight connections from the intersections with the X-axis and bow shock. These are calculated analytically in the model (see SI). (MIDDLE) Histories showing (b) the cumulative distance traveled and (c) energy for the same trajectories with the times of observation and entry at the bow shocked marked for the 15 eV trajectory (d) Mapped electron distributions at locations 1, 10, 30 and 60% of the sheath thickness from the MPB. Colored circles match the trajectories shown in panels (a)-(c). (e) Reproduced from Figure 1(f) (see text for discussion).

5. Results

Figure 3 displays the model results based on the parameter values given above. Individual trajectories are shown in Figure 3a for electrons arriving at an observer located at $\chi = 0.01$, where $\chi = (x - R_{MPB})/(R_{BS} - R_{MPB})$ is the distance from the MPB to the observer normalized by the sheath thickness. At this point the bulk flow velocity has fallen to $0.01 \times 0.3 V_{SW} = 1.35$ km/s. Electrons >15 eV observed here have crossed the distant flank bow shock, only gaining a small amount of energy due to the weak shock potential there, to arrive directly at the observation point. At lower energies, electrons enter at more sunward locations, gain more energy, and then make one or more reflections at the bow shock before arriving at the observer.

Figures 3b and 3c reveal how these low-energy electrons (cf. the black trace corresponding to an arrival energy of 4 eV) get a large energy increase (>200 eV in this case) in crossing the bow shock near the subsolar region, and then lose energy on their path to the observer (from $T = 42$ s at the bow shock to $T = 0$ at the observer). By contrast, an arriving 150-eV electron gained a small energy jump at the bow shock and traveled directly to the observer. Panel (b) shows that low-energy electrons may travel total distances of 20–30 R_{mars}; these paths reduce to <10 R_{mars} and total travel times <5 s at higher energies.

Figure 3d shows the mapped electron distribution function at different locations along the X axis, the dark blue trace corresponding to the trajectories shown in the upper plots for $\chi = 0.01$. For the range of energies plotted here, most trajectories arrive at $\chi = 0.01$ directly from the solar wind through bow shock. At more sunward locations, the dotted portions of the model distributions have a sawtooth appearance. Looking from right to left on, for example, the red trace for $\chi = 0.6$ in the middle of the magnetosheath, the most energetic electrons arrive directly from the bow shock, those below the rightmost (second rightmost) tooth have reflected once (twice) at the shock before arriving at the observer, etc. The sharpness of these teeth is certainly an artifact of the idealized model with its discreet energy jumps. However, the simple action of a cross-shock potential does generate electron beams within the shock transition (Feldman et al., 1983; Scudder et al., 1986). We would expect plasma instabilities and turbulence to shape $f(E)$ to its characteristic flat-top appearance. The low-energy portions of the distribution are filled by electrons similar to the black trace in Figure 3c that are significantly energized at the bow shock and lose most of that energy through trapping and reflections within the cavity formed by the bow shock potential. This portion of phase space is sensitive to those energy changes and the mapping to the core or wings of the solar wind distribution.

Concentrating on the evolution of $f(E)$ with distance, the model qualitatively reproduces the apparent "erosion" at higher energies with increasing penetration toward the MPB, as shown in Figure 3e from Figure 1f. The intuitive explanation for this erosion is the escape of more energetic electrons from the cavity formed by the bow shock shape and potential. This must occur, since the model shows electrons at the highest energies that are not trapped within the cavity (to the right of the no-reflection tooth). These electrons do not lose energy themselves, but are replaced deeper in the sheath by direct access of electrons from the flanks where the energy gain from ϕ^{HT} is weaker. The model does not calculate that escape directly, since particles that have escaped, by definition, will not be seen at the observation point.

6. Conclusions

Within the Martian magnetosheath, the electron mean free path for impact ionization of coronal hydrogen is quite long ($\sim 60 R_{mars}$). We have developed a simple global model to illustrate the electron access to, and escape from, the Martian magnetosheath in the total absence of collisions. The model includes all the relevant physical processes, including stagnation along the Mars-Sun line, the advection of the interplanetary magnetic field outside the Martian bow shock, and an ambipolar potential across the shock transition that varies with location. The model calculates electron trajectories within the cavity formed by that potential, and applies Liouville's theorem to map the electron distribution back to its solar wind origins.

The model successfully demonstrates how the apparent high-energy erosion of the electron spectra with increasing penetration into the magnetosheath is a natural consequence of the entrance, trapping, and escape of solar wind electrons. The results also confirm the relatively short total path lengths and residency times for such sheath electrons, justifying the assumption of collision-free kinematics. Extending the model to electrons with nonzero pitch angles would require evaluation of energy changes associated with any cross-field drifts. However, considering just the parallel motion of such electrons, it is straightforward to show that the path lengths (including gyromotion) and transit times scale $\propto (1 + \tan \alpha_{\text{pitch angle}})$ which is only a factor ~5 even at $\alpha_{\text{pitch angle}} = 75°$.

At or below the magnetic pileup boundary and away from crustal field regions, field lines also ultimately connect through the tailward magnetosheath to the solar wind (Xu et al., 2017). Following the principles of our model, solar wind electrons, including heat flux and energetic particle events, will access the upper atmosphere (Ergun et al., 2016; Liemohn et al., 2006; Sakai et al., 2016) where, via the same Liouville's Theorem principles, their phase space density will be preserved unless collisional altitudes are encountered.

The model also has applicability to the identification and relative location of different boundaries often associated with the pileup boundary (e.g., Dubinin et al., 2008).

Acknowledgments
This work was supported by funds from the NASA MAVEN mission; C. M. was supported by the French Space Agency CNES for the observations obtained with the SWEA instrument. S. J. S. thanks ISSI. All the data used here are accessible in the public mission science center (https://lasp.colorado.edu/maven/sdc/public/).

References

Burgess, D., & Scholer, M. (2015). *Collisionless shocks in space plasmas*. Cambridge, UK: Cambridge University Press.

Connerney, J. E. P., Espley, J. R., DiBraccio, G. A., Gruesbeck, J. R., Oliversen, R. J., Mitchell, D. L., et al. (2015). First results of the MAVEN magnetic field investigation. *Geophysical Research Letters*, *42*, 8819–8827. https://doi.org/10.1002/2015GL065366

Crider, D., Cloutier, P., Law, C., Walker, P., Chen, Y., Acuña, M., et al. (2000). Evidence of electron impact ionization in the magnetic pileup boundary of Mars. *Geophysical Research Letters*, *27*(1), 45–48. https://doi.org/10.1029/1999GL003625

de Hoffmann, F., & Teller, E. (1950). Magneto-hydrodynamic shocks. *Physical Review*, *80*, 692–703. https://doi.org/10.1103/PhysRev.80.692

Dubinin, E., Fraenz, M., Pätzold, M., Halekas, J. S., Mcfadden, J., Connerney, J. E. P., et al. (2018). Solar wind deflection by mass loading in the Martian magnetosheath based on MAVEN observations. *Geophysical Research Letters*, *45*, 2574–2579. https://doi.org/10.1002/2017GL076813

Dubinin, E., Modolo, R., Fraenz, M., Woch, J., Duru, F., Akalin, F., et al. (2008). Structure and dynamics of the solar wind/ionosphere interface on Mars: MEX-ASPERA-3 and MEX-MARSIS observations. *Geophysical Research Letters*, *35*, L11103. https://doi.org/10.1029/2008GL033730

Elliott, H. A., Frahm, R. A., Sharber, J. R., Howard, T. A., Odstrčil, D., Opgenoorth, H. J., et al. (2013). The influence of corotating interaction regions and high speed streams on electrons in the Martian magnetosheath and ionosphere. In G. P. Zank et al. (Eds.), *Solar wind 13*, AIP Conference Proceedings (Vol. 1539, pp. 390–393). https://doi.org/10.1063/1.4811067

Ergun, R. E., Andersson, L. A., Fowler, C. M., Woodson, A. K., Weber, T. D., Delory, G. T., et al. (2016). Enhanced O_2^+ loss at Mars due to an ambipolar electric field from electron heating. *Journal of Geophysical Research: Space Physics*, *121*, 4668–4678. https://doi.org/10.1002/2016JA022349

Feldman, W. C., Anderson, R. C., Bame, S. J., Gary, S. P., Gosling, J. T., McComas, D. J., et al. (1983). Electron velocity distributions near the Earth's bow shock. *Journal of Geophysical Research*, *88*(A1), 96–110. https://doi.org/10.1029/JA088iA01p00096

Feldman, W. C., Anderson, R. C., Bame, S. J., Gosling, J. T., Zwickl, R. D., & Smith, E. J. (1983). Electron velocity distributions near interplanetary shocks. *Journal of Geophysical Research*, *88*(A12), 9949–9958. https://doi.org/10.1029/JA088iA12p09949

Feldman, W. C., Asbridge, J. R., Bame, S. J., Montgomery, M. D., & Gary, S. P. (1975). Solar wind electrons. *Journal of Geophysical Research*, *80*(31), 4181. https://doi.org/10.1029/JA080i031p04181

Ghavamian, P., Schwartz, S. J., Mitchell, J., Masters, A., & Laming, J. M. (2013). Electron-ion temperature equilibration in collisionless shocks: The Supernova remnant-solar wind connection. *Space Science Reviews*, *178*(2-4), 633–663. https://doi.org/10.1007/s11214-013-9999-0

Glassmeier, K.-H. (2017). Interaction of the solar wind with comets: A Rosetta perspective. *Philosophical Transactions of the Royal Society of London Series A*, *375*(2097), 20160256. https://doi.org/10.1098/rsta.2016.0256

Gruesbeck, J. R., Espley, J. R., Connerney, J. E. P., DiBraccio, G. A., Soobiah, Y. I., Brain, D., et al. (2018). The three-dimensional bow shock of Mars as observed by MAVEN. *Journal of Geophysical Research: Space Physics*, *123*, 4542–4555. https://doi.org/10.1029/2018JA025366

Halekas, J. S., Taylor, E. R., Dalton, G., Johnson, G., Curtis, D. W., McFadden, J. P., et al. (2015). The solar wind ion analyzer for MAVEN. *Space Science Reviews*, *195*(1-4), 125–151. https://doi.org/10.1007/s11214-013-0029-z

Hall, B. E. S., Sánchez-Cano, B., Wild, J. A., Lester, M., & Holmström, M. (2019). The Martian bow shock over solar cycle 23-24 as observed by the Mars Express Mission. *Journal of Geophysical Research: Space Physics*, *124*, 4761–4772. https://doi.org/10.1029/2018JA026404

Liemohn, M. W., Frahm, R. A., Winningham, J. D., Ma, Y., Barabash, S., Lundin, R., et al. (2006). Numerical interpretation of high-altitude photoelectron observations. *Icarus*, *182*(2), 383–395. https://doi.org/10.1016/j.icarus.2005.10.036

Masters, A., Schwartz, S. J., Henley, E. M., Thomsen, M. F., Zieger, B., Coates, A. J., et al. (2011). Electron heating at Saturn's bow shock. *Journal of Geophysical Research*, *116*, A10107. https://doi.org/10.1029/2011JA016941

Masters, A., Stawarz, L., Fujimoto, M., Schwartz, S. J., Sergis, N., Thomsen, M. F., et al. (2013). Electron acceleration to relativistic energies at a strong quasi-parallel shock wave. *Nature Physics*, *9*(3), 164–167. https://doi.org/10.1038/nphys2541

Matsunaga, K., Seki, K., Hara, T., & Brain, D. A. (2015). Asymmetric penetration of shocked solar wind down to 400 km altitudes at Mars. *Journal of Geophysical Research: Space Physics*, *120*, 6874–6883. https://doi.org/10.1002/2014JA020757

Mazelle, C. X., Meziane, K., Mitchell, D. L., Garnier, P., Espley, J. R., Hamza, A. M., et al. (2018). Evidence for neutrals-foreshock electrons impact at Mars. *Geophysical Research Letters*, *45*, 3768–3774. https://doi.org/10.1002/2018GL077298

Meziane, K., Mazelle, C. X., Mitchell, D. L., Hamza, A. M., Penou, E., & Jakosly, B. M (2019). A fast Fermi acceleration at Mars bow shock. *Journal of Geophysical Research: Space Physics*, *124*, 5528–5538. https://doi.org/10.1029/2019JA026614

Meziane, K., Mazelle, C. X., Romanelli, N., Mitchell, D. L., Espley, J. R., Connerney, J. E. P., et al. (2017). Martian electron foreshock from MAVEN observations. *Journal of Geophysical Research: Space Physics*, *122*, 1531–1541. https://doi.org/10.1002/2016JA023282

Mitchell, D. L., Mazelle, C., Sauvaud, J. A., Thocaven, J. J., Rouzaud, J., Fedorov, A., et al. (2016). The MAVEN solar wind electron analyzer. *Space Science Reviews*, *200*(1-4), 495–528. https://doi.org/10.1007/s11214-015-0232-1

Mitchell, J. J., & Schwartz, S. J. (2013). Nonlocal electron heating at the Earth's bow shock and the role of the magnetically tangent point. *Journal of Geophysical Research: Space Physics*, *118*, 7566–7575. https://doi.org/10.1002/2013JA019226

Mitchell, J. J., & Schwartz, S. J. (2014). Isothermal magnetosheath electrons due to nonlocal electron cross talk. *Journal of Geophysical Research: Space Physics*, *119*, 1080–1093. https://doi.org/10.1002/2013JA019211

Mitchell, J. J., Schwartz, S. J., & Auster, U. (2012). Electron cross talk and asymmetric electron distributions near the Earth's bowshock. *Annales Geophysicae*, *30*(3), 503–513. https://doi.org/10.5194/angeo-30-503-2012

Pierrard, V., & Lazar, M. (2010). Kappa distributions: Theory and applications in space plasmas. *Solar Physics*, *267*(1), 153–174. https://doi.org/10.1007/s11207-010-9640-2

Sakai, S., Andersson, L., Cravens, T. E., Mitchell, D. L., Mazelle, C., Rahmati, A., et al. (2016). Electron energetics in the Martian dayside ionosphere: Model comparisons with MAVEN data. *Journal of Geophysical Research: Space Physics*, *121*, 7049–7066. https://doi.org/10.1002/2016JA022782

Schwartz, S. J., Thomsen, M. F., Bame, S. J., & Stansberry, J. (1988). Electron heating and the potential jump across fast mode shocks. *Journal of Geophysical Research*, *93*, 12,923–12,931. https://doi.org/10.1029/JA093iA11p12923

Scudder, J. D., Mangeney, A., Lacombe, C., Harvey, C. C., & Wu, C. S. (1986). The resolved layer of a collisionless, high beta, supercritical, quasi-perpendicular shock wave. III - Vlasov electrodynamics. *Journal of Geophysical Research*, *91*, 11,075–11,097. https://doi.org/10.1029/JA091iA10p11075

Spreiter, J. R., Summers, A. L., & Rizzi, A. W. (1970). Solar wind flow past nonmagnetic planets—Venus and Mars. *Planetary and Space Science*, *18*(9), 1281–1299. https://doi.org/10.1016/0032-0633(70)90139-X

Thomsen, M. F., Mellott, M. M., Stansberry, J. A., Bame, S. J., Gosling, J. T., & Russell, C. T. (1987). Strong electron heating at the Earth's bow shock. *Journal of Geophysical Research*, *92*(A9), 10,119–10,124. https://doi.org/10.1029/JA092iA09p10119

Trotignon, J. G., Mazelle, C., Bertucci, C., & Acuña, M. H. (2006). Martian shock and magnetic pile-up boundary positions and shapes determined from the Phobos 2 and Mars Global Surveyor data sets. *Planetary and Space Science*, *54*(4), 357–369. https://doi.org/10.1016/j.pss.2006.01.003

Vignes, D., Mazelle, C., Réme, H., Acuña, M. H., Connerney, J. E. P., Lin, R. P., et al. (2000). The solar wind interaction with Mars: Locations and shapes of the bow shock and the magnetic pile-up boundary from the observations of the MAG/ER Experiment onboard Mars Global Surveyor. *Geophysical Research Letters*, *27*(1), 49–52. https://doi.org/10.1029/1999GL010703

Xu, S., Mitchell, D., Liemohn, M., Fang, X., Ma, Y., Luhmann, J., et al. (2017). Martian low-altitude magnetic topology deduced from MAVEN/SWEA observations. *Journal of Geophysical Research: Space Physics*, *122*, 1831–1852. https://doi.org/10.1002/2016JA023467

References From the Supporting Information

Summers, D., & Thorne, R. M. (1991). The modified plasma dispersion function. *Physics of Fluids B*, *3*(8), 1835–1847. https://doi.org/10.1063/1.859653